

# What drives the velocity dispersion of ionized gas in star-forming galaxies?

Xiaoling Yu,<sup>1,2</sup> Yong Shi,<sup>1,2\*</sup> Yanmei Chen,<sup>1,2</sup> David R. Law,<sup>3</sup> Dmitry Bizyaev,<sup>4,5</sup> Longji Bing,<sup>1,2</sup> Songlin Li,<sup>1,2</sup> Luwenjia Zhou,<sup>1,2</sup> Jianhang Chen,<sup>1,2</sup> Rogemar A. Riffel,<sup>6,7</sup> Rogério Riffel,<sup>8,9</sup> Kai Zhang,<sup>10</sup> Yongyun Chen,<sup>1,2</sup> and Kaike Pan<sup>4</sup>

<sup>1</sup>*School of Astronomy and Space Science, Nanjing University, Nanjing 210093, China*

<sup>2</sup>*Key Laboratory of Modern Astronomy and Astrophysics (Nanjing University), Ministry of Education, Nanjing 210093, China*

<sup>3</sup>*Space Telescope Science Institute 3700 San Martin Drive; Baltimore, MD 21218*

<sup>4</sup>*Apache Point Observatory and New Mexico State University, P.O. Box 59, Sunspot, NM, 88349-0059, USA*

<sup>5</sup>*Sternberg Astronomical Institute, Moscow State University, Moscow 119234, Russia*

<sup>6</sup>*Universidade Federal de Santa Maria, Departamento de Física, CCNE, 97105-900, Santa Maria, RS, Brazil*

<sup>7</sup>*Laboratório Interinstitucional de e-Astronomia - LIneA, Rio de Janeiro, RJ, Brazil*

<sup>8</sup>*Departamento de Astronomia, Universidade Federal do Rio Grandedo Sul - Av. Bento Gonçalves 9500, Porto Alegre, RS, Brazil*

<sup>9</sup>*Laboratório Interinstitucional de e-Astronomia, Rua General José Cristino, 77 Vasco da Gama, Rio de Janeiro, Brazil, 20921-400*

<sup>10</sup>*University of Kentucky Department of Physics and Astronomy 505 Rose Street, Lexington, KY 40506, USA*

Accepted XXX. Received YYY; in original form ZZZ

## ABSTRACT

We analyze the **intrinsic** velocity dispersion properties of 648 star-forming galaxies observed by the **Mapping Nearby Galaxies at Apache Point Observatory (MaNGA)** survey, to explore the relation of intrinsic gas **velocity dispersions** with star formation rates (SFRs), SFR surface densities ( $\Sigma_{\text{SFR}}$ ), stellar masses and stellar mass surface densities ( $\Sigma_*$ ). By combining with high  $z$  galaxies, we found that there is a good correlation between the velocity dispersion and the SFR as well as  $\Sigma_{\text{SFR}}$ . But the correlation between the velocity dispersion and the stellar mass as well as  $\Sigma_*$  is moderate. By comparing our results with predictions of theoretical models, we found that **the energy feedback from star formation processes alone and the gravitational instability alone can not fully explain simultaneously the observed velocity-dispersion/SFR and velocity-dispersion/ $\Sigma_{\text{SFR}}$  relationships.**

**Key words:** galaxies: evolution - galaxies: star formation - galaxies: kinematics and dynamics - galaxies: ISM.

## 1 INTRODUCTION

It is well known that the cosmic star formation rate (SFR) peaks around the redshift of  $\sim 1 - 3$  (Lilly et al. 1996; Madau et al. 1996; Madau & Dickinson 2014; Hopkins & Beacom 2006; Karim et al. 2011; Burgarella et al. 2013; Sobral et al. 2013). A key question is to understand what drives this evolution. Studies of spatially resolved ionized-gas kinematics are powerful tools to characterize the galactic dynamics and their roles in driving the evolution of cosmic star formation.

High gas velocity dispersion seems to be a common feature of galaxies at high redshift. The **supersonic velocity dispersion** implies a highly **turbulent interstellar medium (ISM)** of distant galaxies (Law et al. 2007; Förster Schreiber

et al. 2009; Elmegreen & Burkert 2010; Green et al. 2014; Simons et al. 2017; Johnson et al. 2018). Theoretical and observational studies also suggest that gas of distant galaxies has larger random motions compared to that in low redshift galaxies (Nesvadba et al. 2006; Lehnert et al. 2009, 2013; Green et al. 2010, 2014; Wisnioski et al. 2015; Zhou et al. 2017; Johnson et al. 2018). These highly turbulent motions may play a **crucial** role in star formation (Green et al. 2010, 2014; Federrath & Klessen 2012; Zhou et al. 2017). Since the turbulence in the ISM **decays** quickly, some source of energy is required to **maintain** it (Mac Low et al. 1998; Stone, Ostriker, & Gammie 1998; Mac Low 1999; Green et al. 2014; Johnson et al. 2018). Both external and internal mechanisms have been suggested. The **former** includes gas accretion from the intergalactic medium and minor mergers (Glazebrook 2013), while the latter **invokes** star formation feedback (Lehnert et al. 2009, 2013; Green et al.

\* E-mail: yong@nju.edu.cn

2010, 2014; Le Tiran et al. 2011), initial gravitational collapse (Elmegreen & Burkert 2010), gravitational disk instabilities (Bournaud et al. 2010, 2014; Goldbaum, Krumholz, & Forbes 2015), cloud-cloud collisions in the disk (Tasker & Tan 2009), galactic shear from differential rotation in disk galaxies (Krumholz & Burkhardt 2016) and some combinations of the above effects.

Green et al. (2010, 2014) found that there is a correlation between the star formation rate (SFR) and gas velocity dispersion in both local and high redshift star-forming galaxies. Lehnert et al. (2009, 2013) further showed that the SFR surface density ( $\Sigma_{\text{SFR}}$ ) is also related with the gas velocity dispersion in active star-forming galaxies at  $z \sim 1-3$ , consistent with that star formation feedback supports the high gas velocity dispersions and balances the gravitational force. On the other hand, Johnson et al. (2018) found there is a weak trend between the SFR and gas velocity dispersion for both local and high redshift galaxies. For individual star-forming clumps at  $z \sim 2$ , Genzel et al. (2011) did not found a strong trend between  $\Sigma_{\text{SFR}}$  and gas velocity dispersion either, and suggested that a large-scale release of gravitational energy could induce the global large random motions in high- $z$  galaxies.

In this paper, we took advantage of a large sample of local star-forming galaxies with 2-D spectroscopic data available in Mapping Nearby Galaxies at Apache Point Observatory (MaNGA, Bundy et al. 2015), to investigate the relationship between gas velocity dispersions and star formation rates as well as stellar masses. Compared to other Integral Field Spectroscopy (IFS) surveys, such as Calar Alto Legacy Integral Field Area (CALIFA) survey (Sánchez et al. 2012), Sydney-AAO Multi-object Integral field spectrograph (SAMI) Galaxy Survey (Croom et al. 2012; Bryant et al. 2014), MaNGA covers a wide wavelength range from 3600 to 10300 Å for a sample of eventually 10,000 nearby galaxies. In this work, we used 2700 galaxies already released by MaNGA Product Launch-5 (MPL-5). We further collected the SFR,  $\Sigma_{\text{SFR}}$  and gas velocity dispersion data of high  $z$  galaxies from the literatures.

In section 2, we describe the MaNGA survey, the sample selection criteria and data reduction strategy. Section 3 presents our MaNGA sample results and compares with high redshift samples. We discuss which physical processes may drive turbulence in the ISM, and compare with theoretical models in section 4. In section 5, we summarize our main conclusions. We use the cosmological parameters  $H_0 = 70 \text{ km s}^{-1} \text{ Mpc}^{-1}$ ,  $\Omega_m = 0.3$ ,  $\Omega_\Lambda = 0.7$  throughout this paper.

## 2 DATA

### 2.1 The MaNGA data

The MaNGA survey is one of three core programs in the fourth generation of the Sloan Digital Sky Survey (SDSS-IV) that began on July 1, 2014 and aims to obtain spatially resolved information of nearly 10 000 galaxies by 2020 (Bundy et al. 2015; Law et al. 2015; Drory et al. 2015; Yan et al. 2016a; Blanton et al. 2017), which is observed by the 2.5m Sloan Telescope (Gunn et al. 2006). MaNGA is designed to

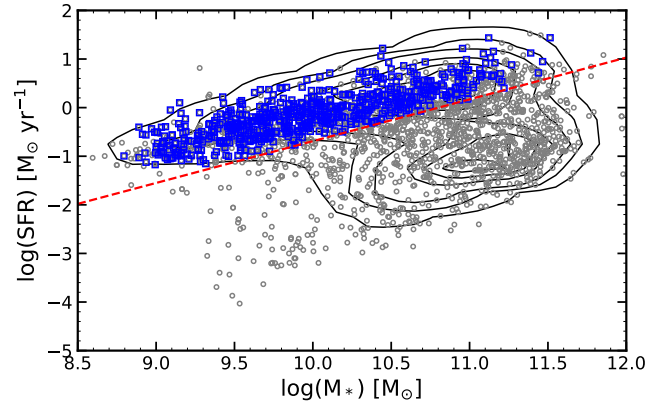


**Figure 1.** The star formation rate (SFR) versus stellar mass diagram of 2360 MaNGA galaxies. Contours show the GSWLC sample. The grey open circles represent 2360 MaNGA galaxies. The red dashed line is adopted as an approximation of the boundary of the star-forming main sequence. The blue open squares represent 648 star-forming galaxies, which the stack spectrums of H $\alpha$  emission lines are fitting well.

investigate the internal kinematic structure and composition of gas and stars for a large sample of nearby galaxies at a spatial resolution of 2.5 arcsec ( $\sim 1 \text{ kpc}$ ). MaNGA employs dithered observations that contain 17 hexagonal bundles of 2'' fibers with five sizes:  $2 \times N_{19}$  (12 arcsec in diameter),  $4 \times N_{37}$ ,  $4 \times N_{61}$ ,  $2 \times N_{91}$ ,  $5 \times N_{127}$  (32 arcsec in diameter). It provides resolved spectroscopy over a wide wavelength range from 3600 to 10300 Å at  $R \sim 2,000$  (Smeed et al. 2013; Yan et al. 2016a; Jin et al. 2016).



The MaNGA sample is volume limited within a redshift range of 0.01  $\sim$  0.15 (Wake et al. 2017), and it is composed of ‘Primary’ and ‘Secondary’ samples based on the spatial extent of the observational coverage. The ‘Primary’ sample contains two thirds of the targets with the observations extended to 1.5  $R_e$  and the ‘Secondary’ sample contains the remaining one third with the observations out to 2.5  $R_e$ . The observations were designed to provide signal to noise ratio of 5 or better in the stellar spectrum within the limits given above (Yan et al. 2016b). The raw data reduction is described in Law et al. (2016). The current study includes 2716 galaxies that have been observed by MaNGA till the summer of 2016, which were from MPL-5.

### 2.2 Sample selection and spectral fitting

We first cross matched our MaNGA galaxies with GALEX-SDSS-WISE Legacy Catalog (GSWLC) (Salim et al. 2016) to obtain the global stellar mass and SFR for 2360 galaxies as shown in Figure 1. The red dashed line is adopted from Fig. 11 of Chang et al. (2015) as an approximation of the boundary (at the  $1\sigma$  level in scatter) of the star-forming main sequence (Chen et al. 2016). Jin et al. (2016) gives the approximately slope and intercept ( $\log \text{SFR} > 0.86 \times \log M_* - 9.29$ ). Totally with 1221 star-forming galaxies. We classified these galaxies into pure star-formation galaxies, AGN and LINERs according to the BPT diagrams with some ex-

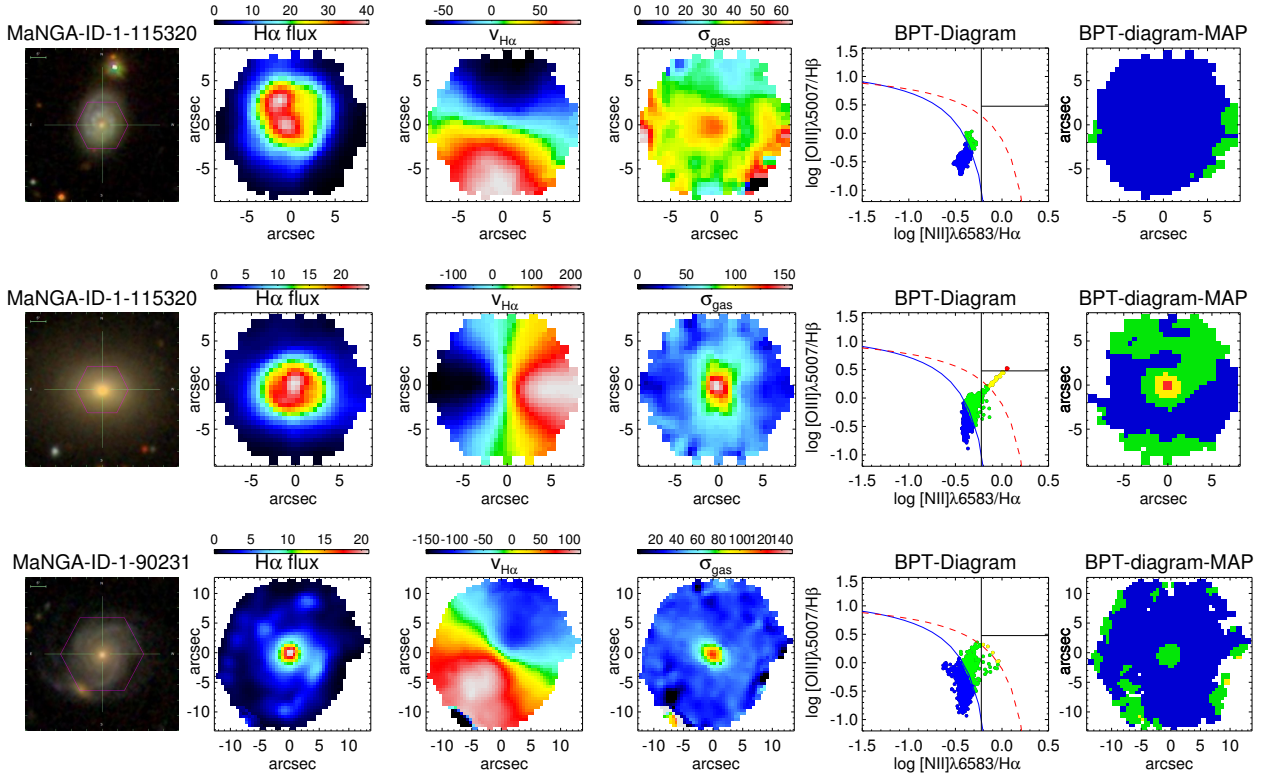


**Figure 2.** Three examples of MaNGA galaxies, which are representative three types of strong H $\alpha$  emission lines. The first column shows the SDSS g, r, i-band image, the H $\alpha$  flux maps are shown in the second column, while the H $\alpha$  flux is in unit of  $10^{-17} \text{erg s}^{-1} \text{cm}^{-2}$ . The third and fourth columns show the gas velocity and gas velocity dispersion fields, respectively. In the third column, the red side is moving away from us and the blue side is approaching. The last two columns show the BPT diagrams and the maps of BPT diagram, while the blue solid curve and the red dashed curve are the boundary of star-formation, composite and AGN regions. The blue region representative star-formation region, the green region representative the composite region. The remaining region is contributed by AGN, while the yellow color and the red color are representative the region of low-ionization nuclear emission regions (LINERs) and Seyferts. The spatial resolved informations (all the flux of emission lines, H $\alpha$  velocity and H $\alpha$  velocity dispersions) are obtained by fitting the emission lines with the MaNGA DAP pipeline (Westfall et al., in preparation).

amples shown in Figure 2 (Baldwin, Phillips, & Terlevich 1981; Kauffmann et al. 2003; Kewley et al. 2006). The fractions of AGN and LINER nature are about 4.42% (52 of 1221). These sources may be influenced by shocks (Kewley et al. 2013; Harrison et al. 2016; Johnson et al. 2018), and their SFRs cannot be estimated accurately. We thus removed them from the further study. Merging galaxies as identified in the SDSS image were excluded further (e.g., the third row in Figure 2). We further selected the galaxies, with **axis ratio** more than 0.5 ( $b/a > 0.5$ ) to focus on relatively face-on galaxies. The axis ratios and effective radius are from the data release by MaNGA ([https://dr15.sdss.org/sas/dr15/manga/spectro/analysis/v2\\_4\\_3/2.2.1/](https://dr15.sdss.org/sas/dr15/manga/spectro/analysis/v2_4_3/2.2.1/)).

For each galaxy in our final selected sample, we stacked the spectrum of all **spaxels** that are not flagged by MaNGA Data Analysis Pipeline (DAP, Westfall et al., in preparation) Pixel Mask to obtain the total flux of each galaxy. During stacking, we didn't shift the emission in the spaxels according to the spatially resolved velocity information. We then fitted it to derive the underlying stellar component with the code of Penalized Pixel-Fitting (pPXF) using MILES templates (Cappellari 2017; Cappellari & Emsellem 2004), as shown in Figure 3. We then used the IDL code

of MPFITEXPR to fit the remaining nebular spectra with single Gaussian profiles as shown in Figure 3. During the fitting, we further **excluded** 98 galaxies with weak emission lines and 48 galaxies with poor fitting. From each fitting, we measured the flux and the ionized gas velocity dispersion of the H $\alpha$  emission lines. At this step, we corrected effect of the beam smearing on the derived velocity dispersion. More details are in section 2.4.1. The final sample contains 648 star-forming galaxies shown as blue open squares in Figure 1.

### 2.3 Star Formation Rate (SFR)

From the spectral fitting, we also derived the H $\alpha$  and H $\beta$  flux to estimate the extinction under the case B (Calzetti 2001). The spatial-resolved SFRs are then estimated from the extinction-corrected H $\alpha$  luminosities (Kennicutt 1998) with a Chabrier IMF (Chabrier 2003):

$$SFR(M_{\odot} \text{year}^{-1}) = 0.56 \times 7.9 \times 10^{-42} L_{\text{H}\alpha, \text{int}} (\text{erg s}^{-1}) \quad (1)$$

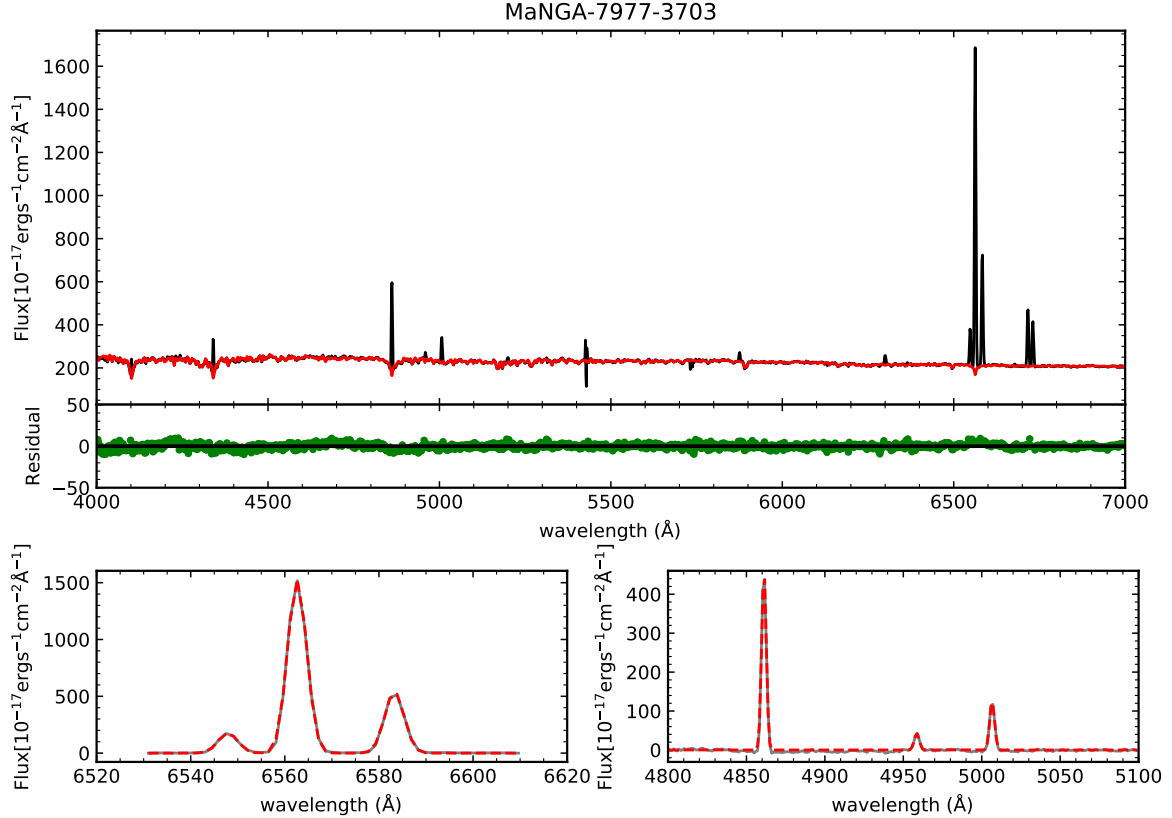


**Figure 3.** Top: An example galaxy of stellar and gas kinematics fit with pPXF. The black line is the relative flux of the observed spectrum. The red line is the pPXF fit for the stellar component. Residuals are presented in the middle plane (green symbols). Bottom: An example galaxy of spectral fitting. The gray line is the stack flux of the observed spectrum. The red dashed line is the best-fitting spectrum of gaussian using IDL code of MPFITEXPR. The left panel shows the  $H\alpha$  region fitting and the right panel shows the  $H\beta$  region fitting.

## 2.4 Gas Velocity Dispersion

Ionized gas velocity dispersion ( $\sigma_{gas}$ ) is measured from the  $H\alpha$  line. The gas velocity dispersion needs to remove the instrumental resolutions, i.e.,  $\sigma_{gas} = (\sigma_{obs}^2 - \sigma_{instr}^2)^{1/2}$ , where  $\sigma_{instr}$  is the instrumental velocity dispersion and  $\sigma_{obs}$  is the observed velocity dispersion. For the single pixel of each galaxy, MaNGA data analysis pipeline provided the  $\sigma_{instr}$ . We used the mean  $\sigma_{instr}$  value of all spaxels.

### 2.4.1 The Effect of Beam Smearing

The measured gas velocity dispersion may be overestimated in the presence of a velocity gradient. As Integral Field Unit (IFU) observations are convolved with the point spread function (PSF), information from each spatial pixel is blended with that of neighbouring regions. This is so called “beam smearing” (Epinat et al. 2010; Davies et al. 2011; Johnson et al. 2018; Zhou et al. 2017). The effect is to artificially increase the observed velocity dispersion, particularly at the dynamical center.

To remove the beam smearing, Green et al. (2010) provided an empirical approach based on the observed velocity map. Following their approach, we first constructed a  $H\alpha$

flux map and its velocity map with five times higher spatial resolution using a linear interpolation according to the observed maps. According to the interpolated flux and velocity maps, we constructed an artificial spectrum with a single gaussian profile at each location. The instrumental resolution is adopted as the velocity dispersion of the model spectrum. Then we convolved this artificial IFU data with a 2D gaussian kernel with the FWHM equal to the seeing for each observation, and binned this high resolution data cube back to the original observational resolution, and measured their velocity dispersion ( $\sigma_{smear}$ ). The final derived dispersion is  $\sigma_{gas,correct} = (\sigma_{gas}^2 - \sigma_{smear}^2)^{1/2}$ . Figure 4 shows the effect of beam smearing on  $\sigma_{gas}$ .

### 2.4.2 The Effect of Instrumental Line Spread Function (LSF)

The spectral resolution of MaNGA is  $50 \sim 80 \text{ km s}^{-1}$  (Bundy et al. 2015). Because of the Instrumental LSF, the  $\sigma_{gas}$  may have large uncertainties or even systematic offsets given inaccurate estimate of the instrumental LSF. The Sydney-AAO Multi-object Integral field spectrograph (SAMi) Galaxy Survey have released the first version data (Green et al. 2018), with a higher spectral resolution of 29



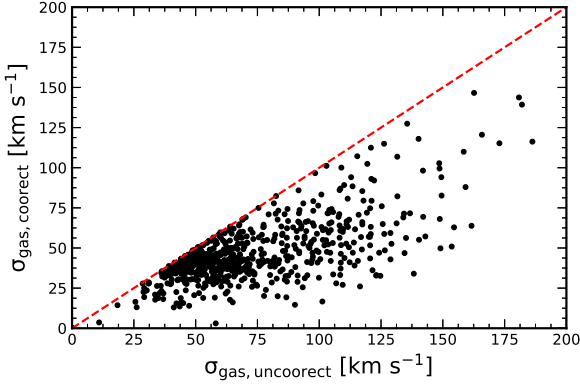


**Figure 4.** Effect of beam smearing on  $\sigma_{gas}$ . We plot the results of modeling the effect of beam smearing on our measure of velocity dispersion and removing it. The x-axis shows the  $\sigma_{gas}$ , which is uncorrected the effect of beam smearing. The y-axis shows the  $\sigma_{gas}$  corrected for beam smearing. The dashed red line shows the one-to-one relation.

$\text{km s}^{-1}$  at 6250 – 7350 (Green et al. 2018; Sharp et al. 2015; Zhou et al. 2017).

For about 150 published SAMI galaxies, we performed the same measurement as MaNGA galaxies, which is to stack the spectrum of all good spaxels, fit the spectrum with pPXF to get the pure H $\alpha$  emission line and fit the profile by a Gaussian curve to derive the velocity dispersion ( $\sigma_{SAMI}$ ). We then degraded the stacked spectra of SAMI galaxies to the MaNGA spectral resolution and derived the line width again ( $\sigma_{SDSS}$ ). Figure 5 plots  $\sigma_{SDSS}/\sigma_{SAMI}$  versus  $\sigma_{SDSS}$  for the SAMI galaxies. A liner function is fitted to the data with the best-fitted result as:

$$\log\left(\frac{\sigma_{SDSS}}{\sigma_{SAMI}}\right) = (-0.21 \pm 0.05)\log(\sigma_{SDSS}) + (0.41 \pm 0.09) \quad (2)$$

As shown in the Figure 5, for  $\sigma_{SDSS}$  larger than 80  $\text{km s}^{-1}$ ,  $\sigma_{SDSS}$  is equal to  $\sigma_{SAMI}$ . For our MaNGA galaxies with  $\sigma_{gas}$  less than 80  $\text{km s}^{-1}$ , we thus used formula (2) to correct the effect of the limited spectral resolution.

## 2.5 Total stellar mass and surface density of stellar mass

We crossmatch GSWLC (Salim et al. 2016) with MaNGA galaxies to obtain the total stellar mass for our sample. The spatially resolved stellar masses are from PIPE3D (Sánchez et al. 2016a,b).

## 3 RESULTS

### 3.1 Results for MaNGA Galaxies

As shown in Figure 9, there is a moderate correlation (Table 1) between the velocity dispersion and the total SFR (top left) and the SFR within MaNGA FOV (top middle), while the relationship with the  $\Sigma_{SFR}$  (top right) is stronger,

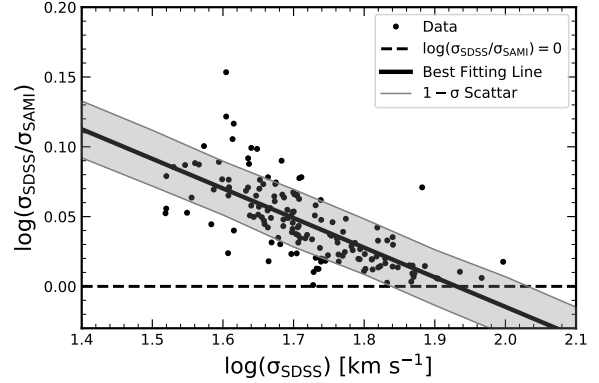


**Figure 5.** The ratio of velocity dispersions measured for SAMI galaxies degraded to the MaNGA resolutions to that at the SAMI resolution. The black solid line refers to the best fitting line of  $\log(\sigma_{SDSS}/\sigma_{SAMI})$  as a function of  $\log(\sigma_{SDSS})$ . The gray shade region refer to the 1 -  $\sigma$  scatter of the best fit line. The black dashed line refers to  $\sigma_{SDSS}/\sigma_{SAMI}$  equal 1.

with a correlation coefficient more than 0.5. There is also a moderate correlation between the velocity dispersion and stellar mass (bottom left and bottom middle), while the relationship with  $\Sigma_*$  is even stronger than that with  $\Sigma_{SFR}$  (see Table 1).

Green et al. (2010) found that the velocity dispersion is correlated with the SFR, but not with the stellar mass or gas fraction. Johnson et al. (2018) analysed about 472  $z \sim 0.9$  star-forming galaxies observed as part of KMOSS Redshift One Spectroscopic Survey (KROSS), and found that the relation between velocity dispersion and SFR was stronger than that between velocity dispersion and stellar mass. For our MaNGA galaxies, we find a good correlation between the velocity dispersion and  $\Sigma_{SFR}$ , and a stronger one with  $\Sigma_*$ .

### 3.2 Results for MaNGA Galaxies and High z Galaxies

In this section, we combined our MaNGA galaxies with those at high redshift. The high  $z$  galaxies are from Wisnioski et al. (2011) ( $z \sim 1.3$ ), Swinbank et al. (2012) ( $z \sim 0.8-2.2$ ), Förster Schreiber et al. (2009) ( $z \sim 2$ ), Cresci et al. (2009) ( $z \sim 2$ ), Lehnert et al. (2013) ( $z \sim 1-3$ ), Law et al. (2009) ( $z \sim 2-3$ ). The KMOS-KROSS sample ( $z \sim 1$ ) is from Johnson et al. (2018). We also included the local DYNAMICS of Newly-Assembled Massive Objects (DYNAMO) sample ( $z \sim 0.1$ ) (Green et al. 2014) and a sample of nearby dwarf galaxies from Moiseev, Tikhonov, & Klypin (2015). Table 2 lists the detailed informations for these studies. From Figure 7 and Table 3, we found that there is a good correlation between velocity dispersion and SFR as well as  $\Sigma_{SFR}$ . But the correlations with stellar mass and  $\Sigma_*$  are much poorer, in contrast to the case when only considering the MaNGA sample, which is likely caused by the limited dynamic range of MaNGA galaxies only.

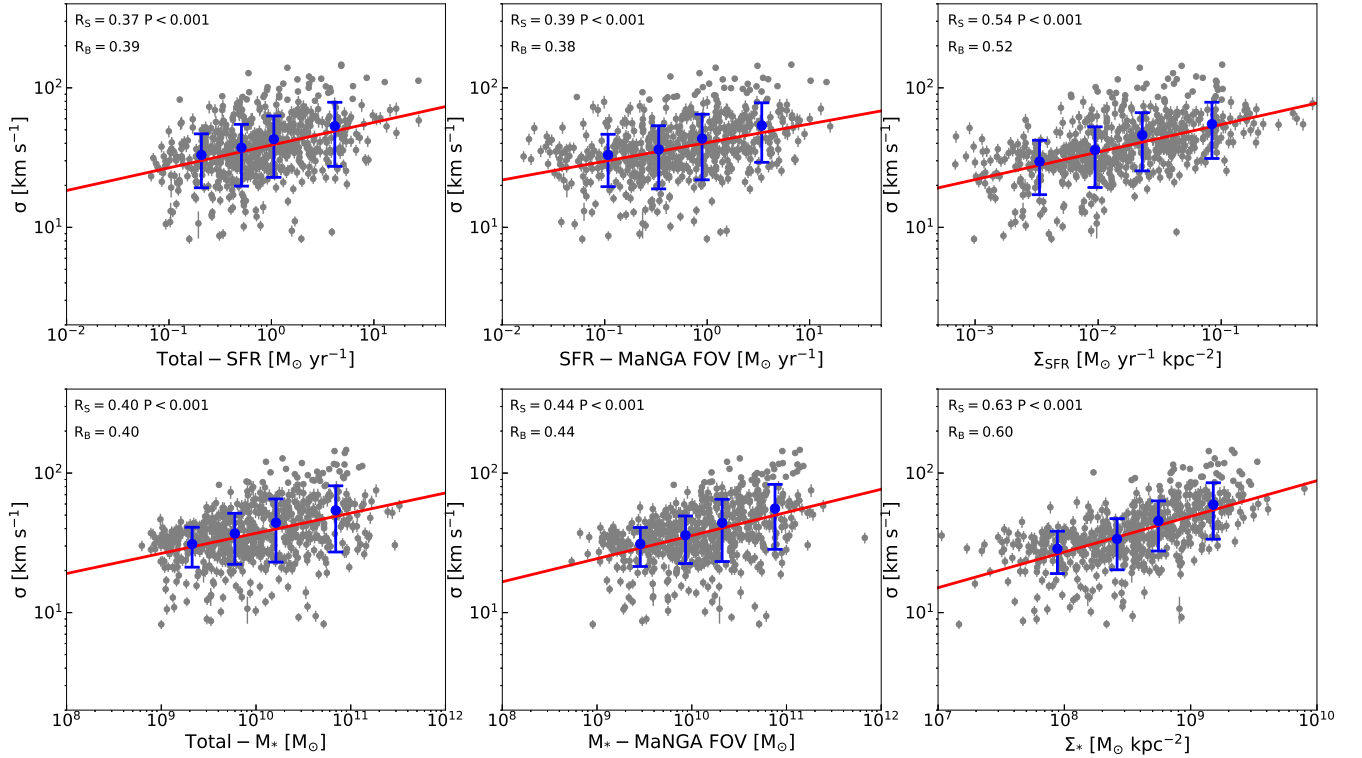


**Figure 6.** Top: Trends between intrinsic gas velocity dispersion and SFR (top left and top middle) as well as  $\Sigma_{\text{SFR}}$  (top right) in section 3.1. The small gray points show all our selected MaNGA sources. The big blue points and error bars show the value of mean  $\sigma$  and standard deviation in x-axis bins (each containing 25 percent of our MaNGA sample). The red solid lines show the best Linear Regression fitting of all our selected MaNGA sources using the method of Kelly (2007). In the upper left corner in each panel,  $R_S$  represents the Spearman correlation coefficient and  $R_B$  represents the corresponding correlation coefficient using the method of Kelly (2007). The Total-SFR from Salim et al. (2016), and the SFR-MaNGA FOV from the emission lines fitting of ( $\text{H}\alpha$  region). The  $\Sigma_{\text{SFR}}$  are converted from SFR-MaNGA FOV. Bottom: Trends between intrinsic gas velocity dispersion and stellar mass (bottom left and bottom middle) as well as  $\Sigma_*$  (bottom right) in section 3.1. All symbols and lines are as same as the top panels. The Total- $M_*$  from Salim et al. (2016). The  $M_*$ -MaNGA FOV and the  $\Sigma_*$  are converted by PIPE3D (Sánchez et al. 2016a,b).

**Table 1.** The results of the linear correlation analysis

	$\sigma$ - SFR			$\sigma$ - $M_*$			$\sigma$ - $\Sigma_{\text{SFR}}$			$\sigma$ - $\Sigma_*$		
	$R_S$	P	$R_B$	$R_S$	P	$R_B$	$R_S$	P	$R_B$	$R_S$	P	$R_B$
MaNGA <sup>a</sup>	0.37	< 0.001	0.39	0.40	< 0.001	0.40	-	-	-	-	-	-
MaNGA <sup>b</sup>	0.39	< 0.001	0.38	0.44	< 0.001	0.44	0.54	< 0.001	0.52	0.63	< 0.001	0.60

a: Stellar mass and SFR are the total Stellar mass and SFR of galaxies from Salim et al. (2016).

b: The SFR and Stellar mass within MaNGA FOV. The  $\Sigma_{\text{SFR}}$  and  $\Sigma_*$  also just cover the observation region of MaNGA.

$R_S$ : Spearman correlation coefficient.

P: Significance level of the Spearman correlation coefficient.

$R_B$ : Correlation coefficient using the method of Kelly (2007)

## 4 DISCUSSION

### 4.1 Which is more fundamental for the relationship with the gas velocity dispersion: SFR or stellar mass?

Many studies in the literature have been done to discuss which one (SFR vs. stellar mass) is better related with the

gas velocity dispersion. We will go through these works in the following and conclude which one may be more fundamental in driving the gas velocity dispersion.

For the relationship between the velocity dispersion and stellar mass, some studies expected this correlation to exist, because velocity dispersions measure the dynamical support of galaxies, regardless of morphological types (Johnson et al.

**Table 2.** List the data sources of detail informations for High z and local galaxies

$ref^{(a)}$	$z$	$\sigma^{(b)}$	$SFR^{(c)}$	$M_*^{(d)}$	$\Sigma_{SFR}$ and $\Sigma_*^{(e)}$	Beam Smearing <sup>(f)</sup>
Wisnioski et al. (2011)	$z \sim 1.3$	$H\alpha$	$H\alpha$	SED Fitting	Re	Yes
Swinbank et al. (2012)	$z \sim 0.8-2.2$	$H\alpha$	$H\alpha$	SED Fitting	Re	Yes
Förster Schreiber et al. (2009)	$z \sim 2$	$H\alpha$	$H\alpha$	SED Fitting	Re	Yes
Cresci et al. (2009)	$z \sim 2$	$H\alpha$	$H\alpha$	SED Fitting	$R_d$	Yes
Lehnert et al. (2013)	$z \sim 1-3$	$H\alpha$	$H\alpha$	—	$R_{iso}$	Yes
Law et al. (2009)	$z \sim 2-3$	$H\alpha$	$H\alpha$	SED Fitting	$R_{ne}$	Yes
KMOS-KROSS(Johnson et al. (2018))	$z \sim 1$	$H\alpha$	$H\alpha$	SED Fitting	Re	Yes
DYNAMO((Green et al. 2014))	$z \sim 0.1$	$H\alpha$	$H\alpha$	SED Fitting	Re	Yes

(a): The references of other high z and local galaxies data sources.

(b): The way of measured gas velocity dispersion.  $H\alpha$  means used  $H\alpha$  emission lines obtain the  $\sigma$

(c): The way of measured SFR.  $H\alpha$  means used  $H\alpha$  emission lines measured the SFR.

(d): The way of measured Stellar Mass. SED Fitting means used the theory of SED Fitting to measure the Stellar Mass

(e): The way of measured  $\Sigma_{SFR}$  and  $\Sigma_*$ , we used the SFR and stellar mass to divide the area within a defined radius to obtain the  $\Sigma_{SFR}$  and  $\Sigma_*$ . Re means the effective radius.  $R_d$  means the radius of the disk scale length.  $R_{iso}$  means the radius of isophotal area (the total area of all pixels above the  $3\sigma$  surface brightness limit of the data).  $R_{ne}$  means radius of nebular emission.

(f): Whether or not considering the effect of beam smearing.

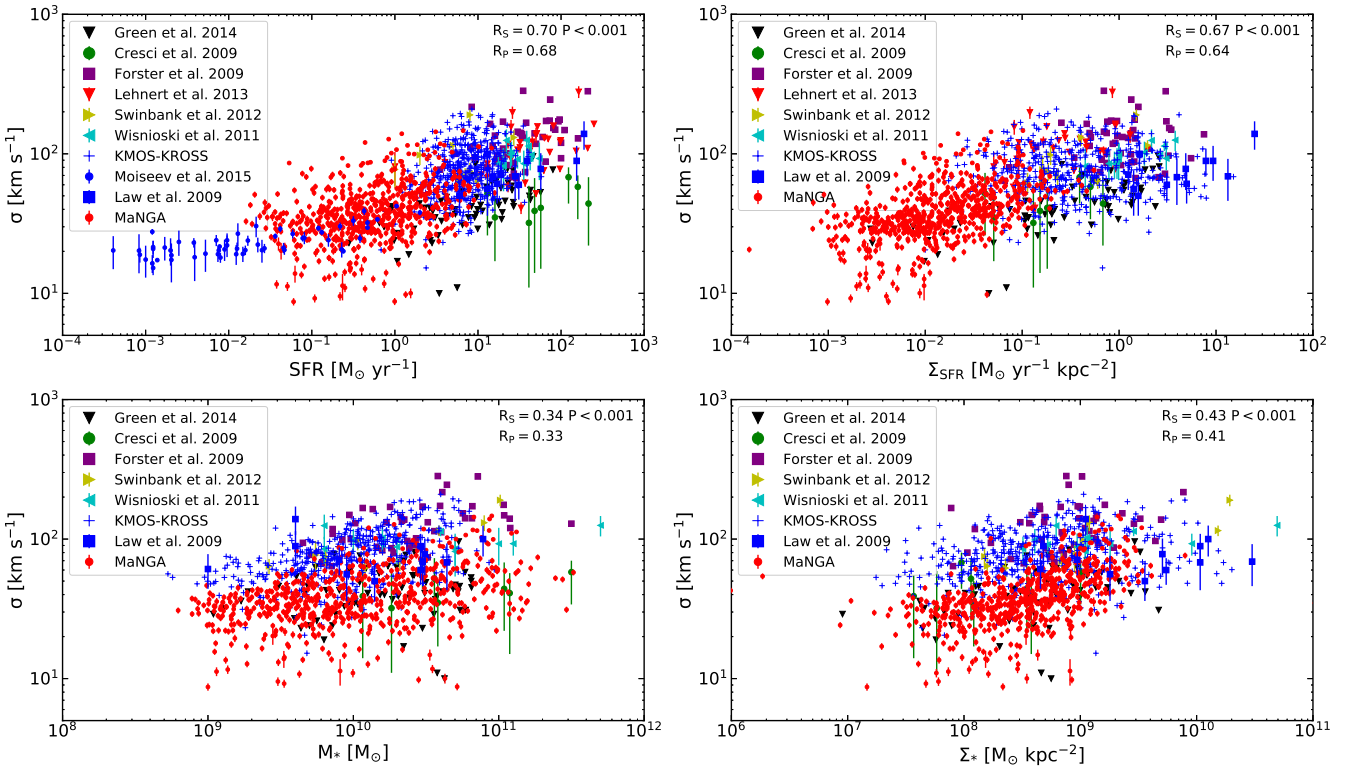


**Figure 7.** Trends between intrinsic gas velocity dispersion ( $\sigma_{gas}$ ) and SFR,  $\Sigma_{SFR}$ , Stellar mass and  $\Sigma_*$  in section 3.2. The high z galaxies are from Wisnioski et al. (2011), Swinbank et al. (2012), Förster Schreiber et al. (2009), Cresci et al. (2009), Lehnert et al. (2013), Gonçalves et al. (2010), Law et al. (2009). The KMOS-KROSS sample is from Johnson et al. (2018). We also combine the local DYNAMO sample (Green et al. 2014) and a sample of dwarf galaxies from Moiseev, Tikhonov, & Klypin (2015). In each panel, the different symbols of the top left corner refer the data from different references.

**Table 3.** The results of the linear correlation analysis

	$\sigma$ - SFR			$\sigma$ - $M_*$			$\sigma$ - $\Sigma_{\text{SFR}}$			$\sigma$ - $\Sigma_*$		
	$R_S$	P	$R_B$	$R_S$	P	$R_B$	$R_S$	P	$R_B$	$R_S$	P	$R_B$
MaNGA + High z	0.70	< 0.001	0.68	0.34	< 0.001	0.33	0.67	< 0.001	0.64	0.43	< 0.001	0.41

$R_S$ : Spearman correlation coefficient.

P: Significance level of the Spearman correlation coefficient.

$R_P$ : Pearson correlation coefficient

2018). Stott et al. (2016) used KROSS sample around redshift of 1.0, and found a weak trend between intrinsic gas velocity dispersion and SFR, also a similarly weak correlation with  $\Sigma_{\text{SFR}}$ , but a moderate correlation is found between the dispersion and stellar mass. They argued that gaseous disks of high redshift star-forming galaxies are significantly different from those in local Universe, with the former showing much hotter dynamics. They suggested that feedback may not be a dominant contributor to their turbulence, but instead the discs may keep their turbulence through ongoing disc instabilities or continuous accretion of cold clumpy gas from the cosmic web (Kereš et al. 2005; Dekel, Sari, & Ceverino 2009). The difference between the work of Stott et al. (2016) and the work of Johnson et al. (2018) is the way to measure the gas velocity dispersion and different theory to remove beam smearing.

Johnson et al. (2018) also used KROSS sample to study the relations of gas velocity dispersion versus stellar mass and SFR. They found that before removing the effect of the beam smearing, the average velocity dispersion increases significantly with the stellar mass. But the relation disappeared after removing the beam smearing, instead the dispersions increase with redshift at fixed stellar masses. There is a weak trend between the intrinsic velocity dispersion and SFR. Their results are consistent with an evolution of galaxy dynamics in which gas-rich disks are increasingly gravitationally unstable at higher redshift.

Green et al. (2010) and Johnson et al. (2018) combined with local galaxies and high z galaxies, and found that the gas velocity dispersions are correlated with their SFRs, but not with their masses or gas fractions. They suggested that star formation is the energetic driver of galaxy disk turbulence at all cosmic epochs. Green et al. (2014) used DY-NAMO sample, combined with high redshift galaxies, and revisited the relation between velocity dispersion and SFR, also found the similar relation.

In our study, the MaNGA survey makes available a much larger sample of nearby galaxies. Combined with high-z samples compiled from the literature, we have a larger sample than previous works. From the results of these wide redshift samples, we found that the relationships of the velocity dispersion with SFR as well as  $\Sigma_{\text{SFR}}$  may be more fundamental than with stellar mass and  $\Sigma_*$ . The latter may be caused by the former combined with the fact that the stellar masses could regulate star formation rates to some extent (Shi et al. 2011, 2018).

## 4.2 Theoretical models to explain the relation between $\sigma_{\text{gas}}$ and SFR

There are two dominant models for the origin of the turbulence: star formation feedback or gravitational instability of the gas (Krumholz & Burkhardt 2016). Both models predict that the velocity dispersions will correlate with their SFRs. The work of Krumholz & Burkhardt (2016) gives the details about these two models.

In Figure 8, we overlaid the gravitational-instability model (left panel) and star-formation-feedback model (right panel). The gravitational-instability model gives SFR as following (Krumholz & Burkhardt 2016):

$$\text{SFR} = \int_{r_0}^{r_1} 2\pi r \epsilon_{\text{ff}} \frac{\Sigma}{t_{\text{ff}}} dr = \frac{16}{\pi} \sqrt{\frac{\phi_P}{3}} \left( \frac{\epsilon_{\text{ff}} v_c^2}{G} \ln \frac{r_1}{r_0} \right) f_g^2 \sigma. \quad (3)$$

where  $v_c$  is the rotational velocity,  $f_g$  is the gas fraction,  $\epsilon_{\text{ff}} = 0.01$  is the SFR per free-fall time,  $\phi_P = 3$  is a factor that accounts for the presence of stars in the disc, and a Coulomb logarithm-like term  $\ln(r_1/r_0)$ , which measures the radial extent of the star-forming disc ( $r_1 = 10, r_0 = 0.1$ ). From equation (3) we find that a gravitational-instability model has a strong dependence on the gas fraction. The star formation feedback model gives the SFR as following (Krumholz & Burkhardt 2016):

$$\text{SFR} = \int_{r_0}^{r_1} 2\pi r \dot{\Sigma}_* dr = \frac{8\sqrt{2}\phi v_c^2}{\pi G Q_g \mathcal{F}} \left( \ln \frac{r_1}{r_0} \right) \left( \frac{P_*}{m_*} \right)^{-1} \sigma^2. \quad (4)$$

where  $Q_g$  is the Toomre parameters of the gas,  $\phi \approx 1$  and  $\mathcal{F} \approx 2$  are constants of order unity that parameterize various uncertainties,  $P_*/m_* = 3000 \text{ km s}^{-1}$  is the momentum per unit mass (Faucher-Giguère, Quataert, & Hopkins 2013). We found that the star formation feedback origin for the turbulence predicts that a velocity dispersion rises more steeply with the SFR, and it does not depend on the gas fraction. For the comparisons with our observations, we give the plausible range of  $f_g$  and  $Q_g$  following with the works of Krumholz & Burkhardt (2016) or Johnson et al. (2018). We also used the rotation velocity  $v_c = 90 - 190 \text{ km s}^{-1}$ , which spans the plausible range for local and high z galaxies. From Figure 8 (right panel), we find that a star-formation-feedback model provides a rather poor match to the observation, while the gravitational-instability model shows better agreement with the observations. Johnson et al. (2018) also test two analytic models but found that both provide an adequate description of the data, and need further observations to rule out either model. In the work of Krumholz & Burkhardt (2016), they also compared with observations and found that gravity is the ultimate source of ISM turbulence, at least in rapidly star-forming, high-velocity dispersion galaxies for which our test is most effective.



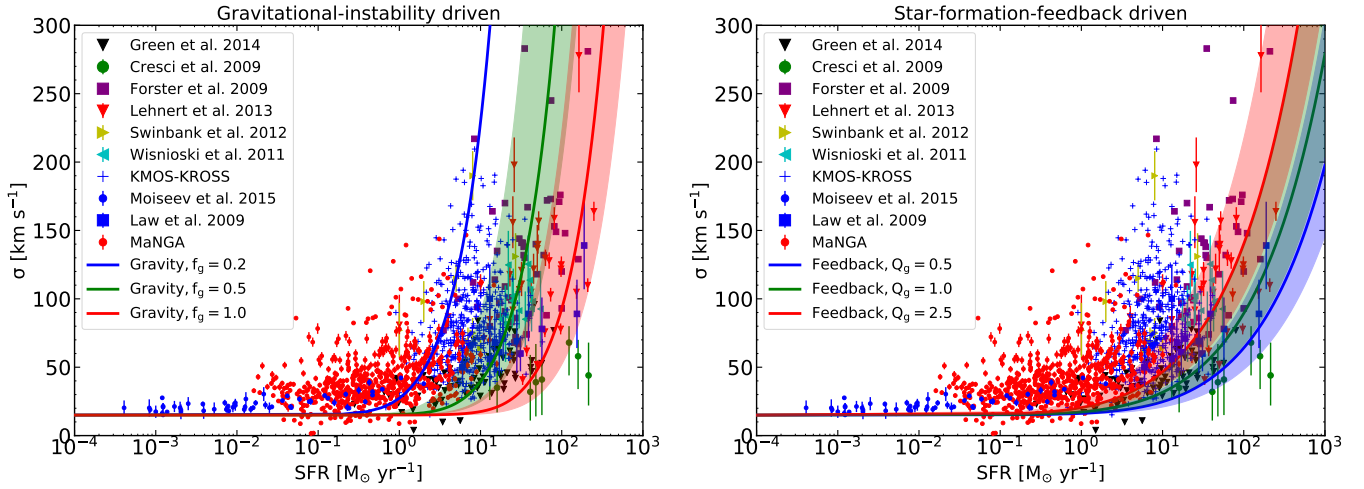


**Figure 8.** The relationship between SFR and gas velocity dispersion. In the left panel, lines show the predictions of the gravitational-instability model (equation 6) for  $f_g = 0.2, 0.5$ , and  $1.0$ , as indicated in the legend. Lines in the right panel show the prediction of the star formation feedback model (equation 8) for  $Q_g = 0.5, 1.0$ , and  $2.5$ . The solid lines are for a circular velocity  $v_c = 140 \text{ km s}^{-1}$  (the median rotation velocity of local and high  $z$  galaxies), and the shaded range shows values from  $v_c = 90 - 190 \text{ km s}^{-1}$ , which spans the plausible range for the local and high-redshift samples. Note that the theoretical model predictions for  $\sigma$  have been added in quadrature with the thermal broadening of HII region about  $15 \text{ km s}^{-1}$ .

The recent work of [Krumholz et al. \(2018\)](#), provided a new model for the structure and evolution of gas in galactic discs. For the relation between  $\sigma$  and SFR, they found that the transport+feedback model is in generally good agreement with the observations at both low and high star formation rates. We compare our MaNGA data with their data and transport+feedback model in Figure 9. It is shown that our MaNGA galaxies locate within the range between local dwarf and local spiral galaxies of their models' predictions (solid lines). A key parameter in their model for dwarf galaxies is the rotation velocity which is adopted to be  $100 \text{ km s}^{-1}$ . Figure 10 shows the distribution of the rotation velocity of our MaNGA galaxies, which is about  $90 \pm 50 \text{ km s}^{-1}$ , consistent with their values for dwarf galaxies. This may explain our galaxies are better fitted by their dwarf-galaxy model. Overall, Figure 9 suggests that the transport+feedback model does a good job in matching our data.

### 4.3 Theoretical models to explain the relation between $\sigma_{gas}$ and $\Sigma_{SFR}$

Figure 11 shows the relationship between  $\sigma_{gas}$  and  $\Sigma_{SFR}$ . We attempt to use theoretical models to explain this relation. If the Jeans instability drives the clumpiness of the disks, there is expected to be a good correlation between the mass of collapsing gas and the gas velocity dispersion ([Elmegreen et al. 2007](#)). Assuming the turbulence is powered by gravity, [Lehnert et al. \(2009\)](#) derived a simple Jeans relationship between gas velocity dispersion and mass:

$$\sigma_{gas} \sim M_J^{1/4} G^{1/2} \Sigma_{gas}^{1/4} = 54 M_{J,9}^{1/4} \Sigma_{SFR}^{0.18} \text{ km s}^{-1} \quad (5)$$

where  $G$  is the gravitational constant,  $M_{J,9}$  is Jeans mass in  $10^9 M_\odot$  and  $\Sigma_{SFR}$  is the surface density of SFR in units

$M_\odot \text{ kpc}^2 \text{ yr}^{-1}$ . In Figure 11, the red solid line shows the relationship between  $\sigma_{gas}$  and  $\Sigma_{SFR}$  of a  $10^8 M_\odot$  giant molecular cloud. Because the masses of our local star-forming galaxies are similar to the Milky Way, the masses of molecular cloud is impossible more than  $10^8 M_\odot$  ([Roman-Duval et al. 2010](#)). So we chose  $10^8 M_\odot$  as the upper limit on the possible contribution of the clumps to the observed velocity dispersion. Figure 11 shows that the velocity dispersion predicted by equation (5) lies below the observed data. [Lehnert et al. \(2009\)](#) obtained the similar results for high  $z$  galaxies. They selected  $10^9 M_\odot$  giant molecular cloud, which is the largest masses estimated for clumps based on spectral energy distribution fitting for high  $z$  galaxies. This comparison implies that the dispersions are not dominated by the self-gravity of the clumps.

[Lehnert et al. \(2009\)](#) pointed that, if star formation dominates the dissipated energy, we may expect a simple scaling law  $\sigma \propto (\epsilon \dot{E})^{1/2}$ , where  $\epsilon$  is the coupling efficiency between the ISM and the energy injection,  $\dot{E}$  is the energy injection due to the star formation. [Dib, Bell, & Burkert \(2006\)](#) noticed that if the coupling efficiency in the ISM modelling is 25 per cent, for galaxies at  $\Sigma_{SFR} = 10^{-2.5}$  to  $10^{-2} M_\odot \text{ yr}^{-1} \text{ kpc}^{-2}$  the disks change from quiescent to starburst ones. In Figure 11, the bottom two solid black lines are derived from  $\sigma_{gas} = 100 \Sigma_{SFR}^{1/2} \text{ km s}^{-1}$  and  $\sigma_{gas} = 140 \Sigma_{SFR}^{1/2} \text{ km s}^{-1}$ , respectively, and the third black solid curve at the top shows  $\sigma_{gas} = 240 \Sigma_{SFR}^{1/2} \text{ km s}^{-1}$  with coupling efficiencies of 100 per cent. If turbulent motions determines the observed velocity dispersions ([Mac Low 1999](#)), we may expect another scaling law  $\sigma \propto (\epsilon \dot{E})^{1/3}$ , where  $\dot{E}$  is the energy dissipated due to turbulence. In Figure 11, the two black dashed lines are derived from  $\sigma_{gas} = 80 \Sigma_{SFR}^{1/3} \text{ km s}^{-1}$  and  $\sigma_{gas} = 130 \Sigma_{SFR}^{1/3} \text{ km s}^{-1}$ , using two scalings for the coupling efficiency, 25 per cent and 100 per cent and a primary in-

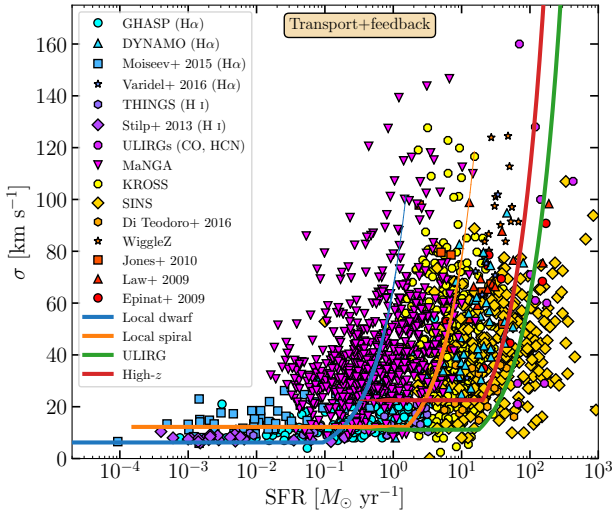


**Figure 9.** Comparison between the observed correlation between gas velocity dispersion and star formation rate and theoretical model. Solid lines represent the theoretical Transport + feedback model for Local dwarf, Local spiral, ULIRG and High- $z$  galaxies. The colored points represent observation datas. The local galaxies are from [Epinat, Amram, & Marcelin \(2008\)](#) (GHASP), [Green et al. \(2010\)](#) (DYNAMO), [Moiseev, Tikhonov, & Klypin \(2015\)](#), [Varidel et al. \(2016\)](#); The HI observations of nearby galaxies from THINGS ([Leroy et al. 2008](#); [Walter et al. 2008](#); [Ianjamasimanana et al. 2012](#)) and Stilp et al. (2013). The nearby ULIRGs observations from [Downes & Solomon \(1998\)](#), [Sanders et al. \(2003\)](#), [Veilleux et al. \(2009\)](#) and [Scoville et al. \(2015, 2017\)](#). The high  $z$  galaxies are from [Epinat et al. \(2009\)](#), [Law et al. \(2009\)](#), [Jones et al. \(2010\)](#), [Di Teodoro, Fraternali, & Miller \(2016\)](#); The WiggleZ sample is from [Wisnioski et al. \(2011\)](#); The SINS sample is from [Wisnioski et al. \(2015\)](#), [Wuyts et al. \(2016\)](#); The KMOS-KROSS sample is from [Johnson et al. \(2018\)](#). Full details about the data are given in Appendix B of [Krumholz et al. \(2018\)](#). The code of this plot is also from [Krumholz et al. \(2018\)](#).

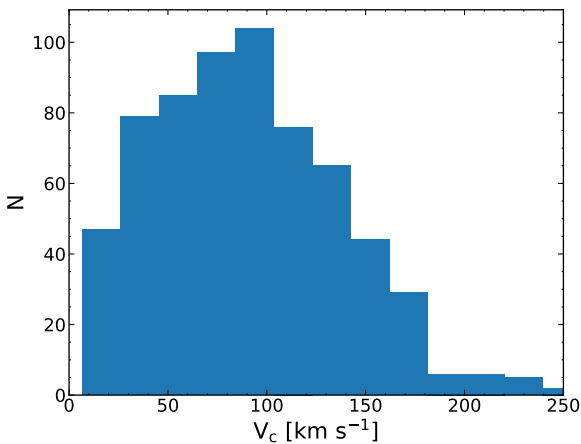


**Figure 10.** The distribution of galaxy rotation curve velocity  $v_c$  for MaNGA galaxies. The mean value is  $v_c = 91.58 \text{ km s}^{-1}$ . The standard deviation of mean value is  $50.83 \text{ km s}^{-1}$ .

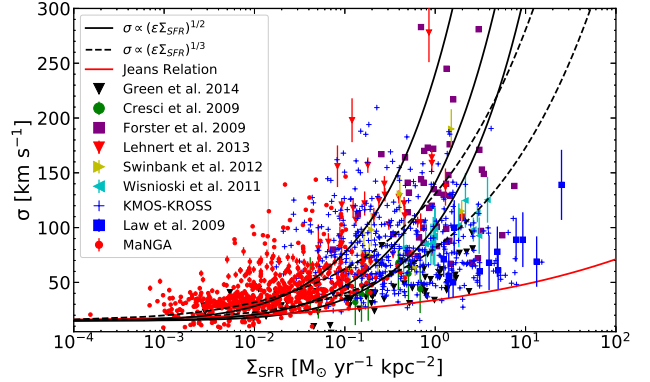


**Figure 11.** Plot of the  $\sigma_{gas}$  vs.  $\Sigma_{SFR}$  in MaNGA sample and other local and high  $z$  galaxies. The symbols for the different samples are shown in the legend to this figure. The solid black lines show that if star formation dominates the dissipated energy, we may expect the relationship of the form  $\sigma \propto (\epsilon \Sigma_{SFR})^{1/2}$ , where  $\epsilon$  is the coupling efficiency between the ISM and the energy injection,  $\dot{E}$  is the energy injection due to the star formation. From bottom to top:  $\sigma_{gas} = 100 \Sigma_{SFR}^{1/2} \text{ km s}^{-1}$ ,  $\sigma_{gas} = 140 \Sigma_{SFR}^{1/2} \text{ km s}^{-1}$  and  $\sigma_{gas} = 240 \Sigma_{SFR}^{1/2} \text{ km s}^{-1}$ . The dashed lines show that if the dispersions correspond to energy dissipation due to turbulent motions, we have  $\sigma \propto (\epsilon \dot{E})^{1/3}$ . From bottom to top:  $\sigma_{gas} = 80 \Sigma_{SFR}^{1/3} \text{ km s}^{-1}$  and  $\sigma_{gas} = 130 \Sigma_{SFR}^{1/3} \text{ km s}^{-1}$ . The red solid line represents the velocity dispersion of a  $10^8 M_\odot$  clump using a simple Jeans relationship. Note that the theoretical model predictions for  $\sigma$  have been added in quadrature with the thermal broadening of HII region about  $15 \text{ km s}^{-1}$ .

jection scale of 1 kpc. From Figure 11 we found that both  $\sigma \propto (\epsilon \Sigma_{SFR})^{1/2}$  and  $\sigma \propto (\epsilon \dot{E})^{1/3}$ , provide an adequate description of the data. But the value of the coupling efficiencies of 100 per cent is an extreme and unrealistic value (the top solid line and the top dashed line in Figure 11). The energy source of turbulence of galaxies with high velocity dispersions may have multiple origins and star formation alone is insufficient to explain it.

## 5 CONCLUSIONS

In this work, we have analyzed the intrinsic velocity dispersion properties of 648 MaNGA star-forming galaxies, and combined them with high  $z$  galaxies. Our main results are as follows:

(1) There is a good correlation between the velocity dispersion and SFR as well as  $\Sigma_{SFR}$ . But there is just a moderate correlation between the velocity dispersion and stellar mass as well as  $\Sigma_*$ .

(2) Comparing theoretical models with observations, because of the different model assumptions, we found that star formation feedback alone and gravitational instability alone can not reproduce the observed two relationships (velocity dispersions vs. SFRs and velocity dispersions vs.  $\Sigma_{SFR}$ ). These different models imply that gas fraction may be an important parameter in this topic.

## ACKNOWLEDGEMENTS

X.Y. and Y.S. acknowledge the support from the National Key R&D Program of China (No. 2017YFA0402704, No. 2018YFA0404502), the National Natural Science Foundation of China (NSFC grants 11825302, 11733002 and 11773013) and the Excellent Youth Foundation of the Jiangsu Scientific Committee (BK20150014). DB is partly supported by RSCF grant 19-12-00145. The authors thank Yifei Jin and Peng Wei for their valuable suggestions. The authors thank Alexei Moiseev for provide his catalog of dwarf galaxies and also thank his valuable suggestions. Funding for the Sloan Digital Sky Survey IV has been provided by the Alfred P. Sloan Foundation, the U.S. Department of Energy Office of Science, and the Participating Institutions. SDSS-IV acknowledges support and resources from the Center for High-Performance Computing at the University of Utah. The SDSS web site is [www.sdss.org](http://www.sdss.org). SDSS-IV is managed by the Astrophysical Research Consortium for the Participating Institutions of the SDSS Collaboration including the Brazilian Participation Group, the Carnegie Institution for Science, Carnegie Mellon University, the Chilean Participation Group, the French Participation Group, Harvard-Smithsonian Center for Astrophysics, Instituto de Astrofísica de Canarias, The Johns Hopkins University, Kavli Institute for the Physics and Mathematics of the Universe (IPMU) / University of Tokyo, Lawrence Berkeley National Laboratory, Leibniz Institut für Astrophysik Potsdam (AIP), Max-Planck-Institut für Astronomie (MPIA Heidelberg), Max-Planck-Institut für Astrophysik (MPA Garching), Max-Planck-Institut für Extraterrestrische Physik (MPE), National Astronomical Observatories of China, New Mexico State University, New York University, University of Notre Dame, Observatório Nacional / MCTI, The Ohio State University, Pennsylvania State University, Shanghai Astronomical Observatory, United Kingdom Participation Group, Universidad Nacional Autónoma de México, University of Arizona, University of Colorado Boulder, University of Oxford, University of Portsmouth, University of Utah, University of Virginia, University of Washington, University of Wisconsin, Vanderbilt University, and Yale University.

## REFERENCES

- Baldwin J. A., Phillips M. M., Terlevich R., 1981, *PASP*, 93, 5  
 Blanton M. R., et al., 2017, *AJ*, 154, 28  
 Bournaud F., Elmegreen B. G., Teyssier R., Block D. L., Puerari I., 2010, *MNRAS*, 409, 1088  
 Bournaud F., et al., 2014, *ApJ*, 780, 57  
 Bryant J. J., Bland-Hawthorn J., Fogarty L. M. R., Lawrence J. S., Croom S. M., 2014, *MNRAS*, 438, 869  
 Bundy K., et al., 2015, *ApJ*, 798, 7  
 Burgarella D., et al., 2013, *A&A*, 554, A70  
 Calzetti D., 2001, *PASP*, 113, 1449  
 Cappellari M., 2017, *MNRAS*, 466, 798  
 Cappellari M., Emsellem E., 2004, *PASP*, 116, 138  
 Cardelli J. A., Clayton G. C., Mathis J. S., 1989, *ApJ*, 345, 245  
 Catinella B., Giovanelli R., Haynes M. P., 2006, *ApJ*, 640, 751  
 Chabrier G., 2003, *PASP*, 115, 763  
 Chang Y.-Y., van der Wel A., da Cunha E., Rix H.-W., 2015, *ApJS*, 219, 8  
 Chen Y.-M., et al., 2016, *NatCo*, 7, 13269  
 Cortese L., et al., 2014, *ApJ*, 795, L37  
 Cresci G., et al., 2009, *ApJ*, 697, 115  
 Croom S. M., et al., 2012, *MNRAS*, 421, 872  
 Davies R., et al., 2011, *ApJ*, 741, 69  
 Dekel A., Sari R., Ceverino D., 2009, *ApJ*, 703, 785  
 Di Teodoro E. M., Fraternali F., Miller S. H., 2016, *A&A*, 594, A77  
 Dib S., Bell E., Burkert A., 2006, *ApJ*, 638, 797  
 Downes D., Solomon P. M., 1998, *ApJ*, 507, 615  
 Drory N., et al., 2015, *AJ*, 149, 77  
 Elmegreen B. G., Burkert A., 2010, *ApJ*, 712, 294  
 Elmegreen D. M., Elmegreen B. G., Ravindranath S., Coe D. A., 2007, *ApJ*, 658, 763  
 Epinat B., Amram P., Balkowski C., Marcelin M., 2010, *MNRAS*, 401, 2113  
 Epinat B., Amram P., Marcelin M., 2008, *MNRAS*, 390, 466  
 Epinat B., et al., 2009, *A&A*, 504, 789  
 Förster Schreiber N. M., et al., 2009, *ApJ*, 706, 1364  
 Faucher-Giguère C.-A., Quataert E., Hopkins P. F., 2013, *MNRAS*, 433, 1970  
 Federrath C., Klessen R. S., 2012, *ApJ*, 761, 156  
 Genzel R., et al., 2011, *ApJ*, 733, 101  
 Glazebrook K., 2013, *PASA*, 30, e056  
 Goldbaum N. J., Krumholz M. R., Forbes J. C., 2015, *ApJ*, 814, 131  
 Gonçalves T. S., et al., 2010, *ApJ*, 724, 1373  
 Green A. W., et al., 2018, *MNRAS*, 475, 716  
 Green A. W., et al., 2010, *Natur*, 467, 684  
 Green A. W., et al., 2014, *MNRAS*, 437, 1070  
 Gunn J. E., et al., 2006, *AJ*, 131, 2332  
 Harrison C. M., et al., 2016, *MNRAS*, 456, 1195  
 Hopkins A. M., Beacom J. F., 2006, *ApJ*, 651, 142  
 Ianjamasimanana R., de Blok W. J. G., Walter F., Heald G. H., 2012, *AJ*, 144, 96  
 Jin Y., et al., 2016, *MNRAS*, 463, 913  
 Johnson H. L., et al., 2018, *MNRAS*, 474, 5076  
 Jones T. A., Swinbank A. M., Ellis R. S., Richard J., Stark D. P., 2010, *MNRAS*, 404, 1247  
 Karim A., et al., 2011, *ApJ*, 730, 61  
 Kassim S. A., et al., 2007, *ApJ*, 660, L35  
 Kauffmann G., et al., 2003, *MNRAS*, 346, 1055  
 Kelly B. C., 2007, *ApJ*, 665, 1489  
 Kennicutt R. C., Jr., 1998, *ARA&A*, 36, 189  
 Kereš D., Katz N., Weinberg D. H., Davé R., 2005, *MNRAS*, 363, 2  
 Kewley L. J., Dopita M. A., Leitherer C., Davé R., Yuan T., Allen M., Groves B., Sutherland R., 2013, *ApJ*, 774, 100  
 Kewley L. J., Groves B., Kauffmann G., Heckman T., 2006, *MNRAS*, 372, 961  
 Krumholz M. R., Burkhardt B., 2016, *MNRAS*, 458, 1671  
 Krumholz M. R., Burkhardt B., Forbes J. C., Crocker R. M., 2018, *MNRAS*, 477, 2716  
 Krumholz M. R., Thompson T. A., 2012, *ApJ*, 760, 155  
 Law D. R., et al., 2016, *AJ*, 152, 83  
 Law D. R., Steidel C. C., Erb D. K., Larkin J. E., Pettini M., Shapley A. E., Wright S. A., 2009, *ApJ*, 697, 2057  
 Law D. R., Steidel C. C., Erb D. K., Larkin J. E., Pettini M., Shapley A. E., Wright S. A., 2007, *ApJ*, 669, 929  
 Law D. R., et al., 2015, *AJ*, 150, 19  
 Le Tiran L., Lehnert M. D., van Driel W., Nesvadba N. P. H., Di Matteo P., 2011, *A&A*, 534, L4  
 Lehnert M. D., Le Tiran L., Nesvadba N. P. H., van Driel W., Boulanger F., Di Matteo P., 2013, *A&A*, 555, A72  
 Lehnert M. D., Nesvadba N. P. H., Le Tiran L., Di Matteo P., van Driel W., Douglas L. S., Chemin L., Bournaud F., 2009, *ApJ*, 699, 1660

- Leroy A. K., Walter F., Brinks E., Bigiel F., de Blok W. J. G., Madore B., Thornley M. D., 2008, *AJ*, 136, 2782
- Lilly S. J., Le Fevre O., Hammer F., Crampton D., 1996, *ApJ*, 460, L1
- Mac Low M.-M., 1999, *ApJ*, 524, 169
- Mac Low M.-M., Klessen R. S., Burkert A., Smith M. D., 1998, *PhRvL*, 80, 2754
- Madau P., Dickinson M., 2014, *ARA&A*, 52, 415
- Madau P., Ferguson H. C., Dickinson M. E., Giavalisco M., Steidel C. C., Fruchter A., 1996, *MNRAS*, 283, 1388
- Moiseev A. V., Tikhonov A. V., Klypin A., 2015, *MNRAS*, 449, 3568
- Nesvadba N. P. H., Lehnert M. D., Eisenhauer F., Gilbert A., Tecza M., Abuter R., 2006, *ApJ*, 650, 693
- Roman-Duval J., Jackson J. M., Heyer M., Rathborne J., Simon R., 2010, *ApJ*, 723, 492
- Sánchez S. F., et al., 2012, *A&A*, 538, A8
- Sánchez S. F., et al., 2016, *RMxAA*, 52, 171
- Sánchez S. F., et al., 2016, *RMxAA*, 52, 21
- Salim S., et al., 2016, *ApJS*, 227, 2
- Sanders D. B., Mazzarella J. M., Kim D.-C., Surace J. A., Soifer B. T., 2003, *AJ*, 126, 1607
- Scoville N., et al., 2017, *ApJ*, 836, 66
- Scoville N., et al., 2015, *ApJ*, 800, 70
- Sharp R., et al., 2015, *MNRAS*, 446, 1551
- Shi Y., Helou G., Yan L., Armus L., Wu Y., Papovich C., Stierwalt S., 2011, *ApJ*, 733, 87
- Shi Y., et al., 2018, *ApJ*, 853, 149
- Simons R. C., et al., 2017, *ApJ*, 843, 46
- Smee S. A., et al., 2013, *AJ*, 146, 32
- Sobral D., Smail I., Best P. N., Geach J. E., Matsuda Y., Stott J. P., Cirasuolo M., Kurk J., 2013, *MNRAS*, 428, 1128
- Stilp A. M., Dalcanton J. J., Skillman E., Warren S. R., Ott J., Koribalski B., 2013, *ApJ*, 773, 88
- Stone J. M., Ostriker E. C., Gammie C. F., 1998, *ApJ*, 508, L99
- Stott J. P., et al., 2016, *MNRAS*, 457, 1888
- Swinbank A. M., Smail I., Sobral D., Theuns T., Best P. N., Geach J. E., 2012, *ApJ*, 760, 130
- Tasker E. J., Tan J. C., 2009, *ApJ*, 700, 358
- Varidel M., Pracy M., Croom S., Owers M. S., Sadler E., 2016, *PASA*, 33, e006
- Veilleux S., et al., 2009, *ApJS*, 182, 628
- Wake D. A., et al., 2017, *AJ*, 154, 86
- Walter F., Brinks E., de Blok W. J. G., Bigiel F., Kennicutt R. C., Jr., Thornley M. D., Leroy A., 2008, *AJ*, 136, 2563
- Wang B., Silk J., 1994, *ApJ*, 427, 759
- Wisnioski E., et al., 2015, *ApJ*, 799, 209
- Wisnioski E., et al., 2011, *MNRAS*, 417, 2601
- Wuyts S., et al., 2016, *ApJ*, 831, 149
- Yan R., et al., 2016, *AJ*, 152, 197
- Yan R., et al., 2016, *AJ*, 151, 8
- Zhou L., et al., 2017, *MNRAS*, 470, 4573

This paper has been typeset from a  $\text{\TeX}/\text{\LaTeX}$  file prepared by the author.